Multifunctional nano-heterogeneous Ni(OH)$_2$/NiFe catalysts on silicon photoanode toward efficient water and urea oxidation

Sol A Lee [a,1], Jin Wook Yang [a,1], Tae Hyung Lee [a], Ik Jae Park [b], Changyeon Kim [a], Sung Hyun Hong [c], Hyungsoo Lee [d], Sungkyun Choi [a], Jooho Moon [d], Soo Young Kim [c], Jin Young Kim [a,*], Ho Won Jang [a,e,**]

[a] Department of Materials Science and Engineering, Research Institute of Advanced Materials, Seoul National University, Seoul 08826, Republic of Korea
[b] Department of Applied Physics, Sookmyung Women's University, Seoul 04310, Republic of Korea
[c] Department of Materials Science and Engineering, Korea University, Seoul 02841, Republic of Korea
[d] Department of Materials Science and Engineering, Yonsei University, Seoul 03722, Republic of Korea
[e] Advanced Institute of Convergence Technology, Seoul National University, Suwon 16229, Republic of Korea
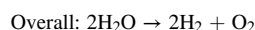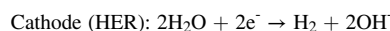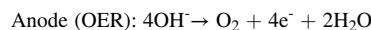
ARTICLE INFO

ABSTRACT

Exploiting inexhaustible free energy from the sun to produce clean and sustainable fuels is an attractive route toward the heavily polluted earth and energy shortage. Photoelectrochemical cell is strategic energy device because the generated fuels can be stored and used on-demand. Herein, we present the fabrication of Si photoelectrodes with efficient charge separation and transfer using metal-insulator-semiconductor heterostructures for energy-rich fuel production via photoelectrochemical water and urea oxidation. With controls of the native SiO$_x$ insulator layer and catalytic NiFe metal layer, Si photoelectrode exhibits a photovoltage of 530 mV and a photocurrent density of 33.3 mA cm^{-2} at 1.23 V versus reversible hydrogen electrode. Further employed Ni(OH)$_2$ catalysts allow Si photoanode to achieve fill factor of 25.73% and solar-to-hydrogen conversion efficiency of 10.8% with a perovskite/Si tandem solar cell. The fabricated Ni(OH)$_2$/NiFe/n-Si photoanode shows considerable performances toward urea oxidation. Our work presents new insights into sunlight-assisted hydrogen production using wastewater.

1. Introduction

Harnessing the sunlight to convert carbon-free and energy-rich hydrogen by photoelectrochemical (PEC) water splitting is one of the solutions to provide clean electricity [1–3]. The semiconductors with moderate bandgap are used as photoelectrodes for light absorption. Under solar illumination, photogenerated electron-hole pairs are separated and transported to the solid/electrolyte interfaces. The electrons are consumed for hydrogen evolution reaction (HER), and holes are employed for oxygen evolution reaction (OER) at the anode. The reaction in alkaline aqueous solution is expressed as the following equation:

Anode (OER): $4OH^- \rightarrow O_2 + 4e^- + 2H_2O$

Cathode (HER): $2H_2O + 2e^- \rightarrow H_2 + 2OH^-$

Overall: $2H_2O \rightarrow 2H_2 + O_2$

The OER, which is a 4-electron-transfer process, is challenging because of sluggish reaction and the requirement of substantial energy of 1.23 V [4], and thus determines the overall PEC efficiency. To deal with it, OER can be conducted with other favorable (photo)electrochemical reactions, which can be triggered at a lower potential. In this regard, urea oxidation reaction (UOR) is a promising reaction since its thermodynamic potential is 0.37 V and the utility of pollutant urea to valuable fuels [5,6]. Various electrocatalysts for urea oxidation have been reported and introduced to photoanodes as cocatalysts to enhance the photocatalytic activity toward urea oxidation [6,7].

An n-type silicon, 2nd abundant element in the earth crust, has been

widely utilized in photovoltaics and microelectronics because of its long carrier lifetime and high crystallinity [8]. Considering the required aspects for the photoelectrode material (i.e., absorption of the solar spectrum, cost-effectiveness, and long carrier diffusion length), Si is a prime candidate to be employed for PEC devices. However, exploiting Si as photoanode is challenging because of its instability in aqueous electrolytes and low catalytic activity [9,10]. The valence band position of silicon is more negative than the oxidation potential (H_2O/O_2), requiring a large applied potential. Also, its theoretical photovoltage is ~750 mV [11], which is insufficient for driving water splitting reaction. In the past decades, many efforts have been devoted to preventing Si from being corroded by introducing protection layers with chemical stability and catalytic activity in alkaline electrolytes [12–15]. Especially, metal-insulator-semiconductor (MIS) architecture is a promising candidate for Si photoanodes. Because MIS structure prevents the surface recombination originating from the metal-induced gap states compared to the direct metal-semiconductor Schottky junction and increase barrier height, leading to the large photovoltage output [16]. To maximize the barrier height, which is the driving force for generating photovoltage, interface engineering of MIS photoanodes has been conducted by inserting ultrathin tunneling oxide layer (e.g., HfO_x, Al_2O_3, TiO_2, SiO_x) using high-vacuum types of equipment [17–21]. The introduction of efficient co-catalysts with optical transparency on MIS photoanode can accelerate the PEC activity at low overpotential. Loget et al. reported the $Si/SiO_x/Ni$ MIS structures with Ni-Prussian blue derivative (NiFePB) [22]. Similar work was done using CoFePB and NiRuPB with inhomogeneity of metal thin film for OER and UOR [23]. Recently, amorphous Ni-Mo-O coatings with the optically adaptive property were introduced on $n-Si/SiO_x/Ni$ MIS photoanodes as UOR catalysts [24]. From an integrated point of view, however, studies on the integrated analysis of MIS photoanodes by engineering each layer, such as the effects of physical/chemical properties of the insulating layer and metal composition on OER and UOR performance, are still intriguing.

In this article, we report the tailored MIS photoanodes for water and urea oxidation and investigate their properties by manipulating the insulating SiO_x layer using chemical etching methods, the composition of Ni_xFe_{1-x} metal thin films, and incorporation of additional $Ni(OH)_2$ catalyst via electrodeposition. We show that the status of the SiO_x layer has a huge effect on the properties of MIS photoanodes. With the native SiO_x insulating layer, composition control of Ni_xFe_{1-x} metal thin film improves the photovoltages and exhibits catalytic activity. A systematic study reveals that introducing additional $Ni(OH)_2$ catalysts on $Ni_{0.5}Fe_{0.5}/SiO_x/n-Si$ leads to a higher fill factor of over 25% and enhances the charge transfer kinetics and stability. With the aids of perovskite/Si tandem solar cell, wired photovoltaic (PV)-PEC tandem device generates a photocurrent of 8.8 mA cm^{-2}, corresponding to the solar-to-hydrogen (STH) conversion efficiency of 10.8% under zero bias. We finally demonstrate that optimized $Ni(OH)_2/Ni_{0.5}Fe_{0.5}/SiO_x/n-Si$ generates high performance toward OER and shows a low onset potential of 0.83 V vs. RHE for UOR. These results indicate the design of efficient MIS photoanodes consisting of abundant materials toward clean H_2 production using urea-containing wastewater.

2. Experimental

2.1. Preparation of substrates

Phosphorous-doped n-Si wafer ((100) oriented, single-side polished, $1-5$ Ω•cm) was cut into 1.5 cm × 1.5 cm pieces. All wafer pieces were cleaned with acetone, isopropanol alcohol, and ultrapure water by ultrasonication. The Si wafers without any etching process were denoted as $SiO_x/n-Si$. To further control the SiO_x layer, first, we conducted a conventional RCA-2 etching process (denoted as $SiO_{x,RCA}/n-Si$); Si pieces were soaked in 3/1 v/v concentrated H_2SO_4/H_2O_2 solution for 10 min, immersed in a buffered HF etchant for 30 sec, and cleaned with DI water. Then wafers were soaked in 5/1/1 (by volume) concentrated

H_2O, hydrochloric acid, and hydrogen peroxide at 80 °C for 30 min. Finally, the Si pieces were rinsed with ultrapure water and dried under a flow of N_2. Second, n-Si wafers were soaked in buffered oxide etchant (7:1, J. T. Baker) for 30 s to remove the residual SiO_x layer (denoted as $SiO_{x,BOE}/n-Si$).

2.2. E-beam deposition of transition metals

Transition metal thin layers were deposited on silicon substrate by electron beam evaporator (Rocky Mountain Vacuum Tech.). Applied e-beam voltage was set at 7.5 kV, and a base pressure was maintained in the range of 10^{-6} Torr. All transition metal thin film layers were deposited with the rate of 0.1–0.2 Å s^{-1}. Ni (Taewon Scientific Co., 99.999%) and Fe (Taewon Scientific Co., 99.999%) evaporation targets were used, and the NiFe alloy targets with various compositions (wt%) were prepared by using an arc furnace.

2.3. Electrodeposition of Ni(OH)₂

To conduct electrodeposition of $Ni(OH)_2$, back side of silicon was scratched and InGa eutectic alloy (Sigma Aldrich) was applied to form an ohmic contact. Then, copper wire was attached on top of the InGa alloy using conductive silver paste. After the silver paste dried, the Si surface except for the deposition area (1 cm × 1 cm) was completely sealed with an adhesive Kapton tape to prevent contact with the electrolyte. Electrodeposition of $Ni(OH)_2$ was conducted in a standard three-electrode system; an encapsulated Si electrode as the working electrode, a Pt mesh as the counter electrode, and a saturated calomel electrode (SCE) as the reference electrode. Electrolytes were prepared by dissolving 0.004 M nickel nitrate hydrate ($NiNO_3•6 H_2O$, Daejung) and 0.01 M potassium nitrate (KNO_3, Daejung) and kept at the temperature of 40 °C. Electrodeposition of $Ni(OH)_2$ was conducted by applying −0.15 mA for 10 s. After electrodeposition, Si pieces were rinsed with deionized water, dried under nitrogen gases, and Kapton tapes were removed.

2.4. Fabrication of perovskite/Si tandem solar cell

For the rear side of the Si cell, 80-nm-thick ITO films were deposited using sputter, and 300-nm-thick Ag electrode was deposited using a thermal evaporator. For the front side of Si cell, 20-nm-thick ITO films were formed as the recombination layer. On top of the ITO/silicon bottom cell, PTAA/perovskite/C_{60} layer was deposited sequentially. PTAA solution (5 mg mL^{-1} in toluene) was spin-coated at 6000 rpm for 25 s, followed by annealing at 100 °C for 10 min. For the preparation of 3D perovskites, solutions were prepared by dissolving formamidinium (FAI), methylammonium bromide (MABr), CsI, PbI_2, and $PbBr_2$. The molar ratio was adjusted to form stoichiometric $FA_{0.65}MA_{0.20}Cs_{0.15})Pb(I_{0.8}Br_{0.2})_3$ in mixed solvent system (DMF:NMP = 4:1 (v/v)). 2D additive perovskite solution was prepared by adding 2 mol% $Pb(SCN)_2$ and 2 mol % PEAX (=I, SCN) to the 3D perovskite solution. The prepared solution was spin-coated at 4000 rpm for the 20 s on PTAA film. To fully crystallize the spin-coated films, it was immersed in diethyl ether (DE) for 30 s. After immersing in DE, the color of the film changed to dark brown, indicating the formation of crystallized perovskite films. The crystallized film was annealed at 100 °C for 10 min. On top of the perovskite, C_{60} layers (C60, bathocuproine (BCP), Ag electrode) were deposited using a thermal evaporator. A 0.2 wt% of PEIE (80% ethoxylated solution) in methyl alcohol was spin-coated at 6000 rpm for 30 s. ITO films were deposited on the C_{60}/PEIE layer using sputtering at room temperature. A 150-nm-thick Ag metal grid was deposited using a thermal evaporator on the ITO film to fabricate final monolithic perovskite/Si tandem cells.

2.5. Characterization

The morphologies and microstructures of samples were analyzed by

field emission scanning microscopy (MERLIN Compact, JEISS) and transmission electron microscopy (JEM-2100 F, JEOL). GIXRD (X′pert Pro, PANalytical) analysis was conducted to confirm the phase of Ni_xFe_{1-x}. X-ray photoelectron spectroscopy (AXIS-His, KRATOS) analysis was performed to investigate the surface bonding of samples. The narrow spectrums were analyzed using CASAXPS software. The reflectance of the sample was determined by UV-Vis (V-770, JASCO). ICP-MS (NexION 350D, Perkin-Elmer) analysis was conducted to confirm the dissolution of Ni_xFe_{1-x} films.

2.6. PEC measurements

PEC measurements were carried out in a three-electrode system using a potentiostat (Ivium nStat, Ivium Technologies) with Pt mesh as a counter electrode and Ag/AgCl (KCl sat.) as a reference electrode. A light source was Xe arc lamp (LS 150, Abet Technologies), and the intensity of the light from the solar simulator with AM 1.5 G filter was calibrated using a reference photodiode (S300, McScience) to be 1 sun (100 mW cm^{-2}). The incident photon-to-current conversion efficiency was measured using a monochromator (MonoRa150) and solar simulator by applying 1.23 V and 1.5 V (vs. RHE). Electrochemical impedance spectroscopy (EIS) was carried out by using the alternating current with an amplitude of 10 mV and applying the onset potential of the samples. The sweeping frequency ranged from 250 kHz to 1 Hz. The Nyquist plots were fit to the equivalent circuit using the Z plot 2.x software. According to the Nernst equation, the measured potential (vs. Ag/AgCl) was converted to the reversible hydrogen electrode (RHE) scale:

$$E_{RHE} = E_{Ag/AgCl} + E^{\circ}_{Ag/AgCl} + 0.059 \times pH$$

where E_{RHE} is the potential versus RHE, $E_{Ag/AgCl}$ is the experimentally measured potential versus Ag/AgCl (KCl sat.), $E^{\circ}_{Ag/AgCl}$ is 0.198 V at 25 °C, and the pH of the 1 M NaOH electrolyte is 14.

The charge injection efficiency (Φ_{inj}) of the sample was calculated using LSV curves in 1 M NaOH with or without 0.5 M Na_2SO_3, where Na_2SO_3 was used as a hole scavenger:

$$J_{PEC} = J_{abs} \times \Phi_{sep} \times \Phi_{inj}$$

$$J_{Na_2SO_3} = J_{abs} \times \Phi_{sep}$$

where J_{PEC} is the measured photocurrent density and J_{abs} is an ideal photocurrent density, assuming that all absorbed photons are converted to current.
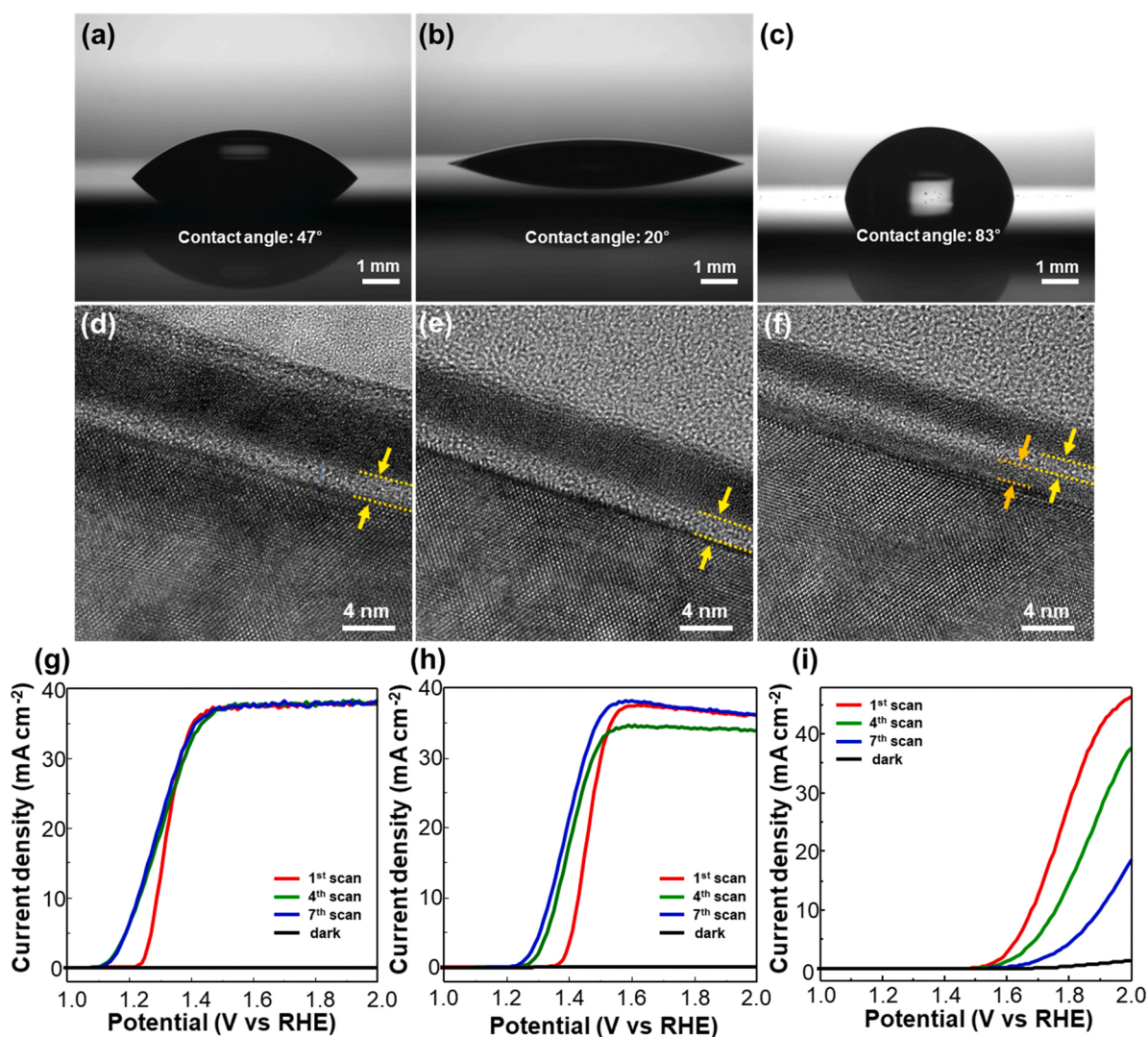
Fig. 1. Effect of controlling SiO_x layer. Contact angles of the silicon substrates; (a) SiO_x/n-Si, (b) $SiO_{x,RCA}$/n-Si, and (c) $SiO_{x,BOE}$/n-Si. Cross-sectional TEM images of the deposited thin films on silicon substrates; (d) Fe/SiO_x/n-Si, (e) Fe/$SiO_{x,RCA}$/n-Si, and (f) Fe/$SiO_{x,BOE}$/n-Si. *J-V* curves of (g) Fe/SiO_x/n-Si, (h) Fe/$SiO_{x,RCA}$/n-Si and (i) Fe/$SiO_{x,BOE}$/n-Si.

3. Results and discussion

3.1. SiO$_x$ control

We prepared three types of SiO$_x$ layers (SiO$_x$, SiO$_{x,RCA}$, SiO$_{x,BOE}$) to investigate the effects of controlling SiO$_x$ on photoelectrochemical (PEC) properties of Si photoanodes. Further details of preparing SiO$_x$ layers are provided in the Experimental Section. Contact angle measurements were conducted to investigate the surface wetting properties of Si substrates with controlled SiO$_x$. As shown in Fig. 1(a)-(c), contact angles of SiO$_x$/n-Si, SiO$_{x,RCA}$/n-Si, and SiO$_{x,BOE}$/n-Si were 47°, 20°, and 83°, respectively. It has been reported that Si completely covered with oxides or –OH terminated Si is hydrophilic and stable while Si-H surface or Si-CH$_x$ is hydrophobic [25,26]. By using chemical etching methods, we obtained Si with different surface termination: SiO$_x$ has oxide cover, SiO$_{x,RCA}$ has –OH terminated surface, and SiO$_{x,BOE}$ has Si-H surface.

Fe thin films were deposited on n-Si substrates with a distinctive SiO$_x$ layer using an e-beam evaporator to form metal-insulator-semiconductor (MIS) structured photoanodes. Fig. S1 shows the x-ray photoelectron spectroscopy (XPS) spectra of Fe thin films on Si, where Fe 2p$_{3/2}$ peak consists of Fe^{3+} (710.3 eV and 713.2 eV) peaks and Fe^{3+} satellite peak (718.8 eV). O 1 s peak can be deconvoluted into three peaks which represent Fe-O (529.6 eV), Fe-O-H (531.4 eV), and H-O-H (533.2 eV) bonding [27–31]. Fig. 1(d)-(f) shows a high-resolution cross-sectional transmission electron microscope (HRTEM) images of Fe/SiO$_x$/n-Si, Fe/SiO$_{x,RCA}$/n-Si, and Fe/SiO$_{x,BOE}$/n-Si interface. Fe thin films were uniformly deposited on the substrates, having a thickness of ~4 nm. The Fe/SiO$_x$/n-Si and Fe/SiO$_{x,RCA}$/n-Si showed a similar SiO$_x$ thickness of 1.5 nm between the Si substrate and Fe film, while Fe/SiO$_{x,BOE}$/n-Si showed damaged interface between Fe layer and Si (orange). It has been reported that HF-treated Si can have a rough silicon surface [32], and the obtained cross-sectional HRTEM image of Fe/SiO$_{x,BOE}$/n-Si shows the increase in roughness of the surface and two distinctive layers compared to SiO$_x$ and SiO$_{x,RCA}$.

The PEC performances of insulating SiO$_x$-controlled photoanodes were investigated by measuring linear sweep voltammetry curves in 1 M NaOH electrolyte under 1sun illumination (100 mW cm^{-2}). All PEC measurements were conducted under the AM 1.5 G using a solar simulator (ABET Technologies). The spectral irradiances of the solar simulator and AM 1.5 G are shown in Fig. S2. Considering the 100% of external quantum efficiency of the system, the integrated current density based on the spectral irradiance of the solar simulator showed a slightly higher current density than AM 1.5 G system. Fig. 1(g) and 1(h) show the J-V curves of Fe/SiO$_x$/n-Si and Fe/SiO$_{x,RCA}$/n-Si, respectively. We define the onset potential as a potential which is required to reach the photocurrent of 1 mA cm^{-2}. Fe/SiO$_x$/n-Si showed an onset potential of 1.14 V vs. RHE, while that of Fe/SiO$_{x,RCA}$/n-Si was 1.26 V vs. RHE, which shifted to the anodic direction. In the case of Fe/SiO$_{x,BOE}$/n-Si, drastic degradation of J-V performance was observed, as shown in Fig. 1 (i), which might have originated from the presence of a defective SiO$_x$ layer as shown in Fig. 1(f). Therefore, it can be observed that the native SiO$_x$ layer can form a proper MIS junction by separating metal and Si, preventing surface recombination.

### 3.2. Composition control of Ni$_x$Fe$_{1-x}$ metal thin film

To evaluate the catalytic effects of the composition of metal thin films on MIS photoanodes for photoelectrochemical water oxidation, the Ni/Fe ratio of metal thin films was controlled by an e-beam evaporator. The performance of MIS photoanode is significantly affected by the thickness of the insulator and metal film, changing the extent of band bending [20]. Therefore, the same thickness of the composition-controlled Ni$_x$Fe$_{1-x}$ thin films was introduced to exclude the thickness-dependent characteristics in MIS photoanodes. The thickness of native SiO$_x$ was fixed to ~ 2 nm, and the metallic Ni$_x$Fe$_{1-x}$ thin films were deposited with ~4 nm thickness. As shown in Fig. S3,

introducing Ni$_x$Fe$_{1-x}$ thin layers on silicon substrates increased the light reflection due to the nature of reflecting light. Targets with Ni/Fe ratio of 1:0. 9:1, 3:1, 1:1, 1:9, and 0:1 were used to control the composition of NiFe thin films on SiO$_x$/n-Si photoanodes. Grazing incidence x-ray diffraction (GIXRD) analysis revealed that e-beam deposited metal thin films on silicon were an amorphous phase (Fig. S4). An n-type semiconductor can form a Schottky junction with high work-function metals [15]. As shown in Fig. S5, the metal's work function was derived by ultraviolet photoelectron spectroscopy (UPS). Ni has a work function of 4.41 eV, Ni$_{0.5}$Fe$_{0.5}$ of 3.8 eV, and Fe of 3.81 eV. As the metal's work function is close to the Fermi level of n-Si, the onset potential shifted to the cathodic direction. We conducted XPS analysis to figure out the chemical states of the metal thin films. As shown in Fig. S6, deconvoluted narrow Ni 2p spectra revealed the presence of metallic Ni^0 peak (852.2 eV) and partial Ni^{2+} peak (854.5 eV) for Ni thin film, and Ni 2p and Fe 2p spectra showed metallic Ni^0 peak (852.5 eV) and Ni^{2+} peak (855 eV) and Fe^{3+} peaks (710.3 eV and 712.4 eV) for Ni$_{0.5}$Fe$_{0.5}$ thin film [33–37].

We prepared Ni$_x$Fe$_{1-x}$ thin films on metallic p^{++}-Si and semiconducting n-Si, respectively, to evaluate electrochemical/photoelectrochemical characteristics. The overpotential of p^{++}-Si was calculated using the potential difference between the required potential to reach 10 mA cm^{-2} and water oxidation potential (1.23 V vs. RHE). As shown in Fig. 2(a), Fe thin films on p^{++}-Si showed a high overpotential of 420 mV compared to that of 300 mV for Ni/SiO$_x$/p^{++}-Si. Through the J-V curves, Ni-rich thin films showed more favorable electrochemical properties for water oxidation than Fe-rich thin films. We converted the polarization curves to Tafel plots to investigate the catalytic activity of Ni$_x$Fe$_{1-x}$ thin films. Fig. 2(b) shows the Tafel slopes of Ni$_x$Fe$_{1-x}$ thin films, in which the linear portion of the curves was used. Ni$_{0.5}$Fe$_{0.5}$/SiO$_x$/p^{++}-Si showed the lowest Tafel slope of 42.46 mV dec^{-1}.

Fig. 2(c) shows the J-V curves of composition-controlled Ni$_x$Fe$_{1-x}$/SiO$_x$/n-Si under 1 sun illumination. Contrary to the J-V curves of Ni$_x$Fe$_{1-x}$/SiO$_x$/p^{++}-Si, the Ni$_x$Fe$_{1-x}$/SiO$_x$/n-Si photoanodes showed different tendency regarding the onset potential (V at 1 mA cm^{-2}). Fe/SiO$_x$/n-Si showed a lower onset potential of 1.14 V vs. RHE compared to that of 1.26 V vs. RHE for Ni/SiO$_x$/n-Si. By manipulating the composition of Ni$_x$Fe$_{1-x}$, the lowest onset potential of 1.02 V vs. RHE was achieved for Ni$_{0.5}$Fe$_{0.5}$/SiO$_x$/n-Si. MIS junction photoanodes can offer sufficient photovoltages by using thin tunnel oxides and appropriate metal with high work function [38]. Photovoltage is defined as the difference between the quasi-Fermi level of electrons and holes. We compared the photovoltages of Ni$_x$Fe$_{1-x}$/SiO$_x$/n-Si by calculating the onset potential (V at 1 mA cm^{-2}) differences between n-Si and p^{++}-Si. As shown in Fig. 2(d), the photovoltage of Ni/SiO$_x$/n-Si was 270 mV, while that of Fe/SiO$_x$/n-Si was 510 mV. By controlling the ratio of Ni and Fe, photovoltage of 530 mV was achieved for Ni$_{0.5}$Fe$_{0.5}$/SiO$_x$/n-Si.

The charge injection efficiency, representing the efficiency of photogenerated holes at the semiconductor-electrolyte interfaces consumed for water oxidation, was derived by the ratio of photocurrent density in 1 M NaOH with and without 0.5 M Na$_2$SO$_3$. As shown in Fig. S7, Ni$_{0.5}$Fe$_{0.5}$/SiO$_x$/n-Si showed the highest charge injection efficiency over 90% at 1.23 V vs. RHE. The stability of MIS-structured Si photoanodes was investigated by conducting chronoamperometry measurements at a potential of 1.5 V versus RHE in 1 M NaOH electrolyte in AM 1.5 G condition. As shown in Fig. S8, Ni/SiO$_x$/n-Si was able to stand 80 h without any remarkable decay of photocurrent density, while Fe/SiO$_x$/n-Si became drastically degraded within 1-hour measurement. Ni$_{0.5}$Fe$_{0.5}$/SiO$_x$/n-Si withstood for 1 h and showed continuous photocurrent decay. Chung et al. reported the activity-stability trend of Fe-M hydr(oxy)oxides and showed the quick dissolution of Fe from the electrolytes, which is well-matched with our results [39]. We performed inductively coupled plasma mass spectroscopy (ICP-MS) analysis to figure out the changes in the Ni$_x$Fe$_{1-x}$ layer before and after stability measurements. We used diluted 1 M NaOH electrolytes before and after stability tests. As shown in Table S1, compared to Ni/SiO$_x$/n-Si with the
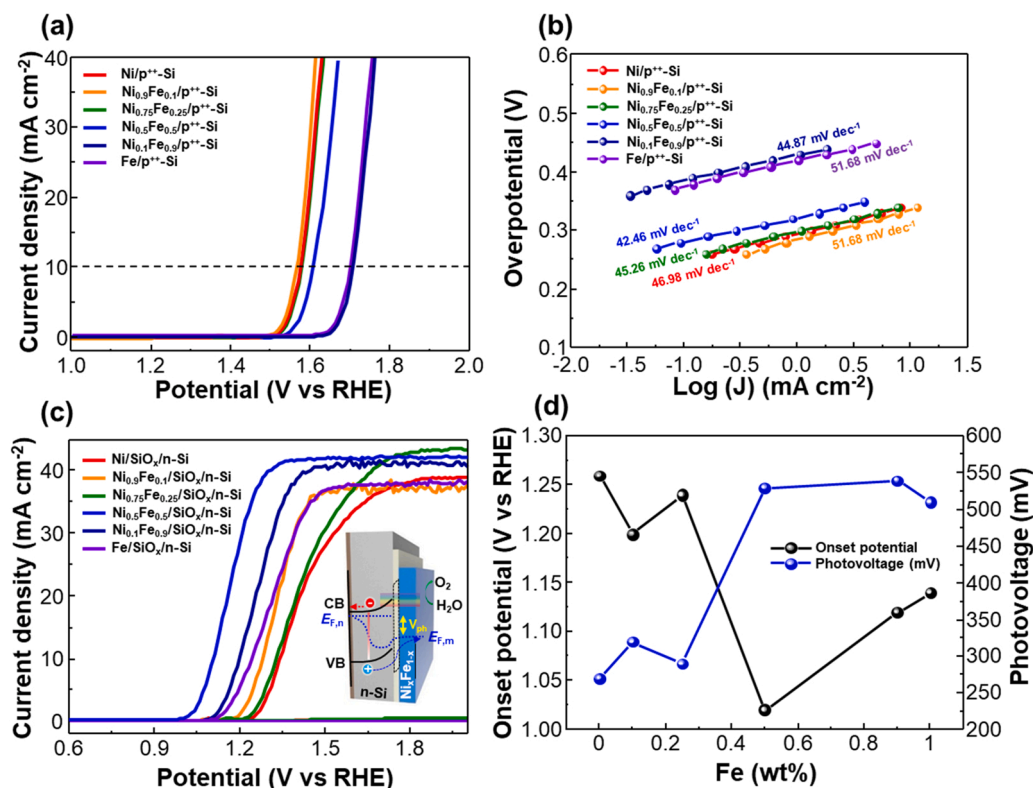
Fig. 2. Electrochemical and photoelectrochemical performances of the Ni_xFe_{1-x} thin film/Si electrodes. (a) Electrochemical performances of the deposited Ni_xFe_{1-x} thin films on p^{++}-Si. (b) Tafel plots of Ni_xFe_{1-x} thin films obtained from the curves in (a). (c) Linear sweep voltammetry curves of Si photoanodes with Ni_xFe_{1-x} thin film catalysts. (d) Comparison of onset potential and photovoltage between $Ni_xFe_{1-x}/SiO_x/n$-Si photoanodes.

negligible change of Ni content, the Fe amount of electrolytes were increased after the stability test of $Fe/SiO_x/n$-Si. Through the stability test and ICP-MS results, it was turned out that Fe itself cannot endure in high alkaline electrolytes. Integrated results showed a trade-off between the onset potential and the stability as adjusting the Ni_xFe_{1-x} composition.

3.3. Electrodeposition of Ni(OH)₂ catalysts for water oxidation

Additional $Ni(OH)_2$ catalysts were introduced on $Ni_{0.5}Fe_{0.5}/SiO_x/n$-Si via cathodic electrodeposition method to expedite water oxidation reaction. We denote the photoanodes as x-$Ni(OH)_2/Ni_{0.5}Fe_{0.5}/SiO_x/n$-Si, where x is the deposition time (seconds). As shown in the photographs of the MIS photoanodes with/without catalysts, the difference was indistinguishable by the naked eyes (Fig. 3(a)). The surface morphology of $Ni(OH)_2$ was analyzed by field emission scanning electron microscopy (FESEM). The faint morphology of 10-$Ni(OH)_2$ was confirmed as shown in Fig. 3(b). As the deposition time increases, the shape of the $Ni(OH)_2$ becomes distinct (Fig. S9). To further characterize the structure of MIS samples, cross-section TEM analysis was conducted. As shown in Fig. 3(c), conformal $Ni_{0.5}Fe_{0.5}$ thin film was formed on top of the SiO_x/Si. The thickness of $Ni_{0.5}Fe_{0.5}$ thin film and SiO_x were 3.5 nm and 1.5 nm, respectively. After the electrodeposition, 3 nm-thick $Ni(OH)_2$ was formed uniformly on $Ni_{0.5}Fe_{0.5}/SiO_x/n$-Si, and the thickness of the SiO_x layer was slightly increased up to 1.8 nm (Fig. 3(d)). A TEM equipped with an energy dispersive spectroscopy (EDS) was conducted to discriminate the elemental distributions of MIS photoanodes. The cross-sectional TEM images and EDS mappings show uniform thin film and Ni, Fe, and O distributions (Fig. S10). The increase of Ni and O signals of 10-$Ni(OH)_2/Ni_{0.5}Fe_{0.5}/SiO_x/n$-Si indicates the presence of $Ni(OH)_2$. The formation of $Ni(OH)_2$ on $Ni_{0.5}Fe_{0.5}/SiO_x/n$-Si was confirmed by XPS analysis, as shown in Fig. S11(a-c). Compared to the XPS spectra of $Ni_{0.5}Fe_{0.5}/SiO_x/n$-Si, the metallic Ni 2p peak disappeared, and only

the Ni^{2+} peak was observed at 855.5 eV. In the case of O 1 s spectra, a significant M-OH peak was found at 530.9 eV.

The PEC performances of the MIS photoanodes with or without catalysts were evaluated in 1 M NaOH electrolyte under simulated 1 sun illumination in the three-electrode system. Fig. 4(a) shows the *J-V* characteristics of the $Ni_{0.5}Fe_{0.5}/SiO_x/n$-Si photoanode with/without catalysts. The onset potential of $Ni_{0.5}Fe_{0.5}/SiO_x/n$-Si photoanode was 1.02 V vs. RHE, and photocurrent density of 33.3 mA cm^{-2} was recorded at 1.23 V vs. RHE. After introducing 10-$Ni(OH)_2$ catalysts on $Ni_{0.5}Fe_{0.5}/SiO_x/n$-Si photoanode, the 10-$Ni(OH)_2/Ni_{0.5}Fe_{0.5}/SiO_x/n$-Si showed 220 mV negative onset potential than the water oxidation potential and the saturated current density of 41 mA cm^{-2}, which reveals that thickness of the $Ni(OH)_2$ is adequate to display the catalytic property without disturbing light absorption of silicon. After the LSV measurements, $Ni(OH)_2/Ni_{0.5}Fe_{0.5}$ catalysts on SiO_x/n-Si maintained the same chemical status as shown in Fig. S11(d-f). We calculated the half-cell solar-to-hydrogen conversion efficiencies (HC-STH) of photoanodes from their LSV curves. As shown in Fig. S12(a), the maximum HC-STH of 10-$Ni(OH)_2/Ni_{0.5}Fe_{0.5}/SiO_x/n$-Si photoanode reaches 2.5% at 1.13 V vs. RHE without buried junction, which exceeds the MIS photoanode without $Ni(OH)_2$ catalysts (1.5% at 1.14 V vs. RHE). As the thickness of $Ni(OH)_2$ increased, the height of the oxidation peak increased (Fig. S12 (b)). Since the thick $Ni(OH)_2$ layer disturbs the light absorption of Si, the saturated current density of x-$Ni(OH)_2/Ni_{0.5}Fe_{0.5}/SiO_x/n$-Si decreased from 40 mA cm^{-2} to 27 mA cm^{-2} while a slight change of onset potential was observed.

A factor indicating the cell's power efficiency is represented as a fill factor (FF). Fill factor is a concept used in photovoltaic and refers to the ratio of the product of current and voltage at the maximum output point to the product of short circuit current and open circuit voltage. From the rectangularity at the maximum power point, we calculated the FF of the photoanodes by deriving the rectangularity of the *J-V* property, followed by the equation:
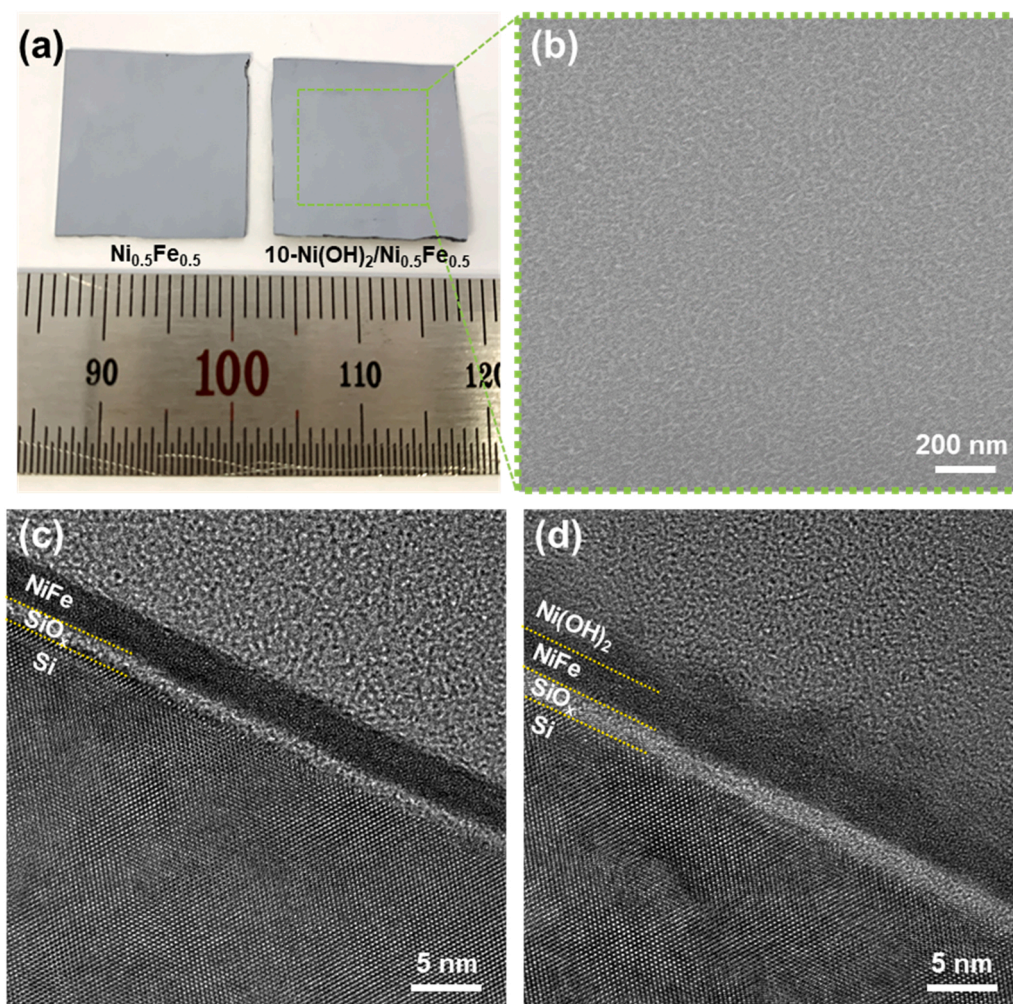
Fig. 3. Morphology of the Si photoanodes. (a) Optical image of $Ni_{0.5}Fe_{0.5}/SiO_x/n$-Si and 10-Ni$(OH)_2/Ni_{0.5}Fe_{0.5}/SiO_x/n$-Si photoanodes. (b) FESEM image of 10-Ni$(OH)_2/Ni_{0.5}Fe_{0.5}/SiO_x/n$-Si. TEM images of (c) $Ni_{0.5}Fe_{0.5}/SiO_x/n$-Si and (d) 10-Ni$(OH)_2/Ni_{0.5}Fe_{0.5}/SiO_x/n$-Si photoanodes.

$$FF = \frac{I_{MP} \times (1.23 - V_{MP})}{I_{SC} \times (1.23 - V_{ON})}$$

where the I_{MP} and V_{MP} are the current density and potential at the maximum power point, I_{SC} is the photocurrent density at 1.23 V vs RHE and E_{ON} is the onset potential. The power efficiency of the photoanode produced by applying FF to the photoelectrode was calculated. When the Ni$(OH)_2$ catalysts were introduced on $Ni_{0.5}Fe_{0.5}/SiO_x/n$-Si, FF was about 25.73%, showing an increase in efficiency by about 8% compared to the $Ni_{0.5}Fe_{0.5}/SiO_x/n$-Si. The increase of FF is advantageous in view of shifting the working potential toward a cathodic direction, leading to the construction of efficient pn PEC cells [40].

To investigate the electrochemical activity of the catalysts, we prepared the same catalysts on metallic p^{++}-Si, as shown in Fig. 4(b). Prepared Ni$(OH)_2/Ni_{0.5}Fe_{0.5}/SiO_x/p^{++}$-Si showed the overpotential (at 10 mA cm^{-2}) of 320 mV, which was 60 mV lower than that of $Ni_{0.5}Fe_{0.5}/SiO_x/p^{++}$-Si, expediting the OER activity. To investigate charge transport properties, electrochemical impedance spectroscopy (EIS) measurement was conducted near the onset potential of each photoanode (Fig. 4(c)). In the Nyquist plot, small semicircles represent the fast charge transfer kinetics of the photoanodes at the interface. The equivalent circuit which was used to fit the measured EIS spectra is shown in the inset. The equivalent circuit components are charge transfer resistance (R_{ct}) and capacitance element (C). The $R_{ct,1}$ represents the contact resistance of silicon, $R_{ct,2}$ the resistance between silicon and catalysts, and $R_{ct,3}$ the resistance between catalysts and electrolytes.

The fitted values of resistance and capacitance of MIS photoanodes with/without catalysts are summarized in Table S2. By introducing catalysts, the smaller charge transfer resistance ($R_{ct,3}$) of the 10-Ni$(OH)_2/Ni_{0.5}Fe_{0.5}/SiO_x/n$-Si resulted in enhanced interfacial charge transfer.

Incident photon-to-current conversion efficiencies (IPCE) of MIS photoanodes with/without catalysts were conducted to investigate the effect of introducing Ni$(OH)_2$ catalysts. The IPCEs of the Si photoanodes were measured in 1 M NaOH electrolyte at an applied bias of 1.5 V vs. RHE, where photoanodes reach the saturated current density. As shown in Fig. 4(d), both Si photoanodes showed the photo-response over the visible wavelength, which is well matched to the bandgap of silicon. By introducing Ni$(OH)_2$ catalysts, 10-Ni$(OH)_2/Ni_{0.5}Fe_{0.5}/SiO_x/n$-Si photoanode reached a value up to 90%, indicating high responsivity to the visible lights. The stability of the 10-Ni$(OH)_2/Ni_{0.5}Fe_{0.5}/SiO_x/n$-Si photoanode was evaluated under 1 sun illumination (100 mW cm^{-2}) in 1 M NaOH (pH 14) and 1 M K-borate (pH 9.5) electrolytes. Compared to the stability of MIS photoanode without Ni$(OH)_2$ catalysts (Fig. S8(b)), 10-Ni$(OH)_2/Ni_{0.5}Fe_{0.5}/SiO_x/n$-Si photoanode showed improved stability up to 5 h (Fig. S13(a)). However, the rapid photocurrent drop was observed after 5 h, which is attributed to the instability of Fe in the alkaline electrolytes (Fig. S8(c)). The fast photocurrent decay of 10-Ni$(OH)_2/Ni_{0.5}Fe_{0.5}/SiO_x/n$-Si photoanode was significantly alleviated in mild alkaline 1 M K-borate electrolyte. As shown in Fig. 4(e), the decrease in photocurrent was not observed for 100 h operation at a constant potential of 1.8 V vs. RHE. After a continuous 100 h
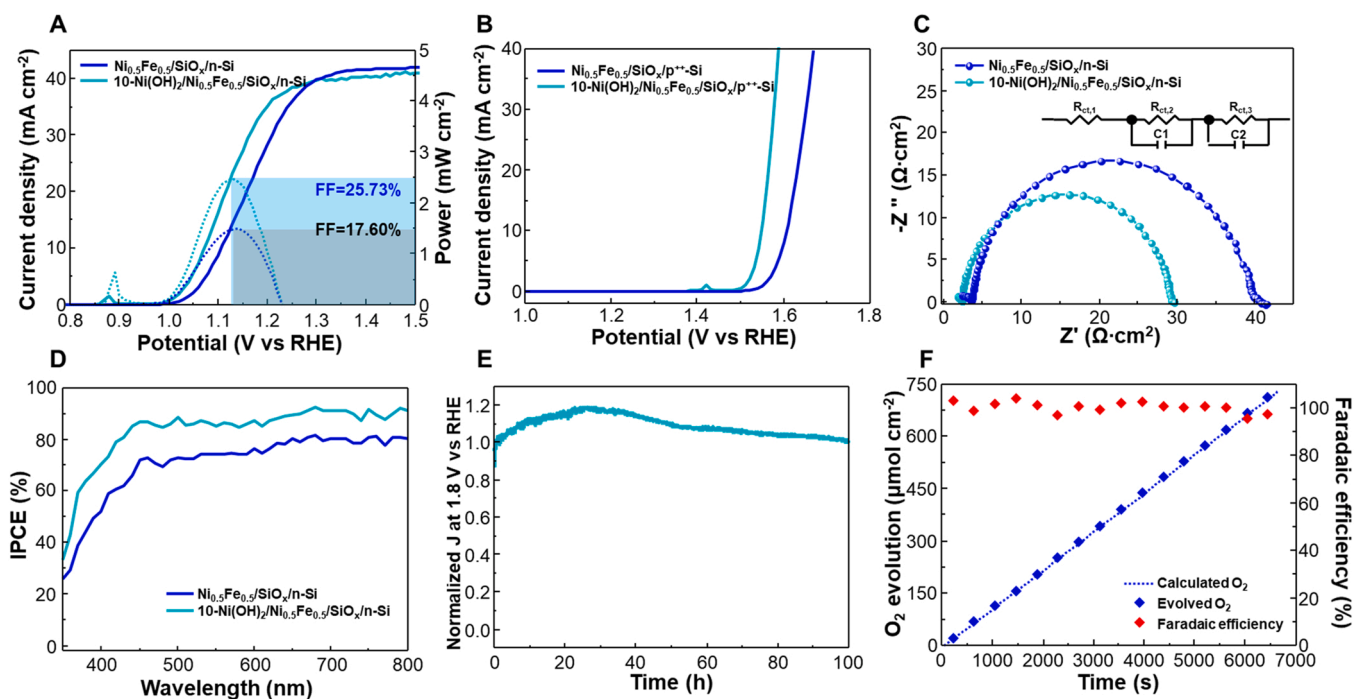
Fig. 4. Water oxidation performances. LSV curves of (a) n-Si photoanodes and (b) p^{++}-Si anodes for water oxidation. (c) Nyquist plots of photoanodes. Inset shows the equivalent circuit. (d) IPCEs of Si photoanodes. (e) Stability test of 10-Ni(OH)$_2$/Ni$_{0.5}$Fe$_{0.5}$/SiO$_x$/n-Si in 1 M K-borate. (f) Faradaic efficiency and O$_2$ evolution of 10-Ni(OH)$_2$/Ni$_{0.5}$Fe$_{0.5}$/SiO$_x$/n-Si.

chronoamperometric measurement, slight degradation in PEC performance was confirmed (Fig. S13(b)). By comparing the stability in alkaline electrolytes with different pH, it can be derived that corrosion of Ni(OH)$_2$/Ni$_{0.5}$Fe$_{0.5}$ can be largely suppressed in the mild electrolyte. To further investigate whether photogenerated charge carriers are consumed for oxygen evolution reaction, the oxygen evolution of 10-Ni(OH)$_2$/Ni$_{0.5}$Fe$_{0.5}$/SiO$_x$/n-Si photoanode was measured by gas chromatography at 1.8 V vs. RHE. As shown in Fig. 4(f), the Faradaic efficiency value was close to 100% during the measurements, which indicates that all photogenerated holes are consumed for water oxidation without any side reactions. A few points showed higher than 100%, attributed to the generated O$_2$ bubbles attached to the photoanode surface. The measured amount of oxygen increased in proportion to time, consistent with the calculated theoretical amount of oxygen generation.

The photovoltage is a driving force to induce spontaneous PEC water splitting without an external bias. Through a series of experiments, optimized MIS photoanodes with oxygen evolving catalysts, generating a photovoltage of 500 mV. However, still, the generated photovoltage is not ample for spontaneous water splitting reaction. The design of devices such as PV-electrolyzer (EC), PV-PEC, and PEC-PEC tandem cells has been considered as a promising approach to achieve clean hydrogen without applying bias [41–45]. To make up for insufficient photovoltage output of Si photoanodes, we fabricated wired perovskite/Si tandem solar cell with the photoanode to supply ample photo-induced voltage. The schematic shown in Fig. 5(a) demonstrated that both solar cell and photoanode were in parallel light illumination with an area ratio of 1:1. The structure of the monolithic perovskite/Si tandem solar cell is illustrated in Fig. S14(a). By designing an optimal bandgap configuration of 1.7 eV/1.12 eV as light absorbers, perovskite/Si tandem solar cell showed the open circuit voltage (V$_{oc}$) of 1.8 V and the short circuit current of 19.3 mA cm^{-2} (Fig. S14(b)) [46]. Under the two-electrode system, *J-V* curves of perovskite/Si tandem solar cell and 10-Ni(OH)$_2$/Ni$_{0.5}$Fe$_{0.5}$/SiO$_x$/n-Si photoanode are shown in Fig. 5(b). The intersection of *J-V* curves indicates achievable photocurrent (operating
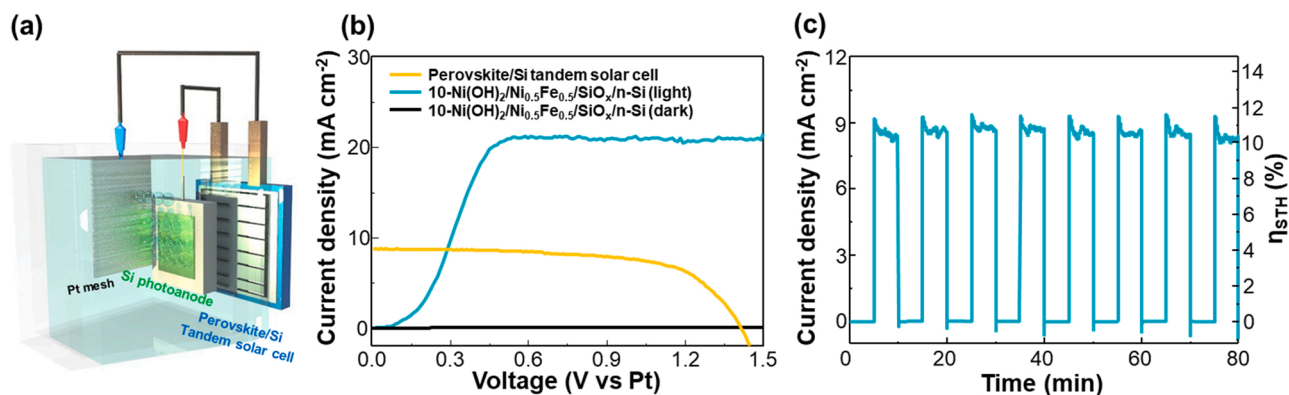
Fig. 5. PV-PEC tandem cell configuration and PEC performance. (a) Schematic of wire-connected tandem cell. (b) 2-electrode *J-V* curves of the 10-Ni(OH)$_2$/Ni$_{0.5}$Fe$_{0.5}$/SiO$_x$/n-Si photoanode and perovskite/Si tandem solar cell under AM 1.5G irradiation. (c) Chronoamperometry of unassisted water splitting under 1 sun illumination.
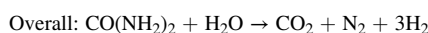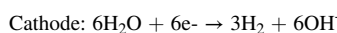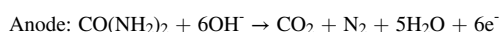
current, J_{op}) without applying external bias. We can estimate the solar-to-hydrogen (STH) conversion efficiency (η_{STH}) of the PV-PEC tandem device using this point by the following equation:

$$\eta_{STH} = \frac{1.23 \quad V \quad \times \quad J_{op} \quad (mA \quad cm^{-2})}{100 \quad mW \quad cm^{-2}}$$

The expected η_{STH} of PV-PEC tandem device is 10.77% by using J_{op} of 8.75 mA cm^{-2}. The actual unassisted water splitting performance of the PV-PEC tandem device was characterized by chronoamperometry measurements at zero bias with chopped light. As shown in Fig. 5(c), the current density of 8.8 mA cm^{-2} is achieved without external bias and practical η_{STH} matches to 10.8% during operation for 80 min.

3.4. Catalysts of urea oxidation reaction

Urea oxidation reaction (UOR) is one of the promising reactions in the view of hydrogen production and pollutant treatment [47]. Similar to the water electrolysis, urea electrolysis produces H_2 at the cathode using the electrical current. At the anode side, the urea oxidation reaction produces CO_2 and N_2 instead of O_2 evolution. The overall urea electrolysis reaction is presented as the following equation:

Anode: $CO(NH_2)_2 + 6OH^- \rightarrow CO_2 + N_2 + 5H_2O + 6e^-$

Cathode: $6H_2O + 6e^- \rightarrow 3H_2 + 6OH^-$

Overall: $CO(NH_2)_2 + H_2O \rightarrow CO_2 + N_2 + 3H_2$

The theoretically required voltage for urea splitting is 0.37 V which is quite lower than that of water splitting (1.23 V) [48]. Urea is a naturally abundant source, originating from fertilizers, urines, industrial production wastes, and so on. The oxidation of urea is advantageous for its relatively low volatility, high energy density (16.9 mJ L^{-1}) in liquid fuels, and high solubility [49]. Although UOR is a complicated

6-electron transfer process [6], urea can be used as sacrificial agents and more easily oxidized species in the water electrolysis electrolytes to overcome sluggish water oxidation reaction [5]. The inclusion of urea in the electrolytes can be considered as natural electrolytes. We investigated the EC/PEC UOR performance of fabricated MIS photoanodes. Fig. 6(a) shows *J-V* curves of p^{++}-Si electrodes for UOR in 1 M NaOH + 0.33 M urea, where 0.33 M of urea is approximately the average molar concentration of urea in human urine [5]. Similar to the activity of OER, Ni/SiO$_x$/p^{++}-Si showed a large urea oxidation peak, while Fe/SiO$_x$/p^{++}-Si didn't show any UOR property. The CV curves of p^{++}-Si demonstrated the (Fig. 6(b)). Fig. 6(c) shows the LSV curves of n-Si photoanodes in the same electrolytes (1 M NaOH + 0.33 M urea). Compared to the electrochemical UOR properties of p^{++}-Si, 10-Ni (OH)$_2$/Ni$_{0.5}$Fe$_{0.5}$/SiO$_x$/n-Si showed the lowest onset potential of 0.83 V vs RHE, which indicates that additional Ni(OH)$_2$ catalyst is efficient not only for OER but also for UOR. Fe/SiO$_x$/n-Si showed the onset potential of 1.13 V vs. RHE, similar to that of water oxidation (1.14 V vs. RHE). From the results, it can be estimated that Fe is not the appropriate catalyst for UOR. HC-STH conversion efficiencies for UOR were calculated based on the *J-V* curves of Si photoanodes. As shown in Fig. 6(d), the stability of 10-Ni(OH)$_2$/Ni$_{0.5}$Fe$_{0.5}$/SiO$_x$/n-Si gradually decreased within 30 min, while 5 h stability was recorded in 1 M NaOH electrolytes as shown in Fig. S13(a). We compared the chronoamperometric curves of UOR (at 1 V vs. RHE in 1 M NaOH + 0.33 M urea) and OER (at 1.23 V vs. RHE in 1 M NaOH) of Si photoanodes to evaluate transient photocurrent decay. When the light was switched on, Si photoanodes showed a photocurrent spike and exponentially decayed to the steady-state during UOR, while the overshoots were not observed during OER (Fig. 6(e)). The presence of a photocurrent spike was the result of photogenerated electron-hole recombination. From the results, the UOR activity of Si photoanodes was hindered by charge recombination, which accelerates the degradation of the stability. We calculated the transient decay time from a logarithmic plot of parameter D, following
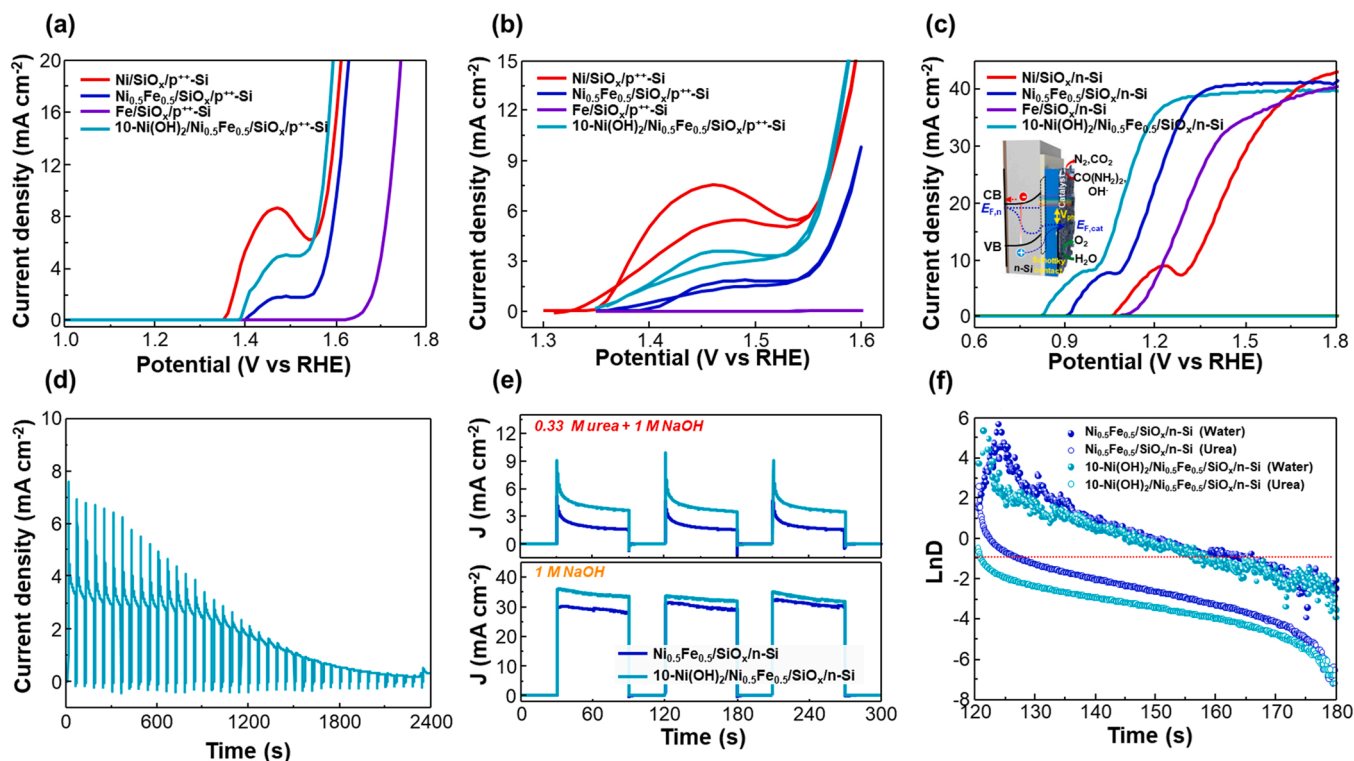
Fig. 6. Electrochemical and photoelectrochemical urea oxidation performances. (a) *J-V* curves and (b) CV curves of p^{++}-Si anodes for urea oxidation in 1 M NaOH + 0.33 M urea. (c) LSV curves of n-Si photoanodes and (d) Chronoamperometry curve of 10-Ni(OH)$_2$/Ni$_{0.5}$Fe$_{0.5}$/SiO$_x$/n-Si measured at 1 V vs RHE in 0.33 M urea +1 M NaOH electrolyte under 1 sun illumination with chopped light. (e) Comparison of chronoamperometry of photoanodes with chopped light under AM 1.5G. (f) ln D-time curve. The transient time constant is defined as the time when ln D = −1.

by the equation:

$$D = \frac{(I_t - I_s)}{(I_m - I_s)}$$

where I_t is the photocurrent at a time (t), I_m and I_s are the photocurrent spike and steady-state photocurrent, respectively. The transient decay time is defined when $\ln D = -1$. Fig. 6(f) shows that both Si photoanodes showed similar transient decay times for water oxidation reaction. However, in the case of UOR, the transient decay time decreased compared to that of OER, and introducing $Ni(OH)_2$ contributes to the charge recombination, although it shifted the onset potential of 90 mV compared to the $Ni_{0.5}Fe_{0.5}/SiO_x/n$-Si.

By integrating the OER and UOR performances of Si photoanodes in the view of photovoltages and onset potentials, composition controlled $Ni_{0.5}Fe_{0.5}$ and electrodeposited $Ni(OH)_2$ catalysts are active toward both reactions, as shown in Fig. S15.

4. Conclusion

We demonstrated the interface engineering of MIS photoanodes and investigated their PEC water and urea oxidation performances. First, we prepared different insulating SiO_x layers by chemical etching method ($SiO_{x,RCA}$, $SiO_{x,BOE}$) and showed that control of SiO_x layer between a metal layer and semiconducting n-Si affected the surface status and interface properties, influencing the PEC performances. Second, we showed that composition control of metallic Ni_xFe_{1-x} thin films shows opposite properties with electrochemical properties and photo-electrochemical properties, where Ni-rich films showed lower over-potentials for EC water oxidation. However, Fe-rich films showed lower onset potentials for PEC water oxidation. There was a trade-off between the stability and the onset potentials depending on the presence of Fe. The optimized $Ni_{0.5}Fe_{0.5}/SiO_x/n$-Si photoanodes showed a high photo-current density of 33.3 mA cm^{-2} at 1.23 V vs. RHE. By introducing additional $Ni(OH)_2$ catalysts on $Ni_{0.5}Fe_{0.5}/SiO_x/n$-Si photoanodes, enhanced fill factor over 25% and external quantum efficiency of 90% was achieved. By introducing perovskite/Si tandem solar cell as a voltage supplier, wired tandem cell device generated an operating photocurrent density of 8.8 mA cm^{-2}, corresponding to the STH conversion efficiency of 10.8%. Lastly, we also investigated PEC urea oxidation properties of Si photoanodes. The heterogeneous $Ni(OH)_2/$ $Ni_{0.5}Fe_{0.5}/SiO_x/n$-Si photoanode showed a highly active urea oxidation property, showing the potential of Si photoanodes for an additional utility of anodic reactions. Although some issues such as stability that must be solved still remain in view of adjusting for industrial applications, these findings suggest the design of efficient MIS photoanodes to produce hydrogen in polluted water.

CRediT authorship contribution statement

Sol A. Lee: Conceptualization, Methodology, Investigation, Writing – original draft, Writing – review & editing, Visualization. **Jin Wook Yang:** Conceptualization, Methodology, Investigation, Writing – original draft, Writing – review & editing, Visualization. **Tae Hyung Lee:** Investigation. **Ik Jae Park:** Methodology, Investigation. **Changyeon Kim:** Investigation. **Sung Hyun Hong:** Investigation. **Hyungsoo Lee:** Investigation. **Sungkyun Choi:** Investigation. **Jooho Moon:** Supervision. **Soo Young Kim:** Supervision. **Jin Young Kim:** Conceptualization, Supervision. **Ho Won Jang:** Conceptualization, Writing – review & editing, Supervision.

Declaration of Competing Interest

The authors declare that they have no known competing financial interests or personal relationships that could have appeared to influence the work reported in this paper.

Appendix A. Supplementary material

Supplementary data associated with this article can be found in the online version at doi:10.1016/j.apcatb.2022.121765.

References

[1] D. Bae, B. Seger, P.C.K. Vesborg, O. Hansen, I. Chorkendorff, Strategies for stable water splitting: via protected photoelectrodes, Chem. Soc. Rev. 46 (2017) 1933–1954, https://doi.org/10.1039/c6cs00918b.

[2] M.S. Prévot, K. Sivula, Photoelectrochemical tandem cells for solar water splitting, J. Phys. Chem. C 117 (2013) 17879–17893, https://doi.org/10.1021/jp405291g.

[3] S.S.M. Bhat, S.A. Lee, T.H. Lee, C. Kim, J Park, T.W. Lee, S.Y. Kim, H.W. Jang, All-solution-processed $BiVO_4/TiO_2$ photoanode with $NiCo_2O_4$ nanofiber cocatalyst for enhanced solar water oxidation, ACS Appl. Energy Mater. 3 (2020) 5646–5656, https://doi.org/10.1021/acsaem.0c00607.

[4] T.H. Lee, S.A. Lee, H. Park, M.J. Choi, D. Lee, H.W. Jang, Understanding the enhancement of the catalytic properties of goethite by transition metal doping: critical role of O* formation energy relative to OH* and OOH*, ACS Appl. Energy Mater. 3 (2020) 1634–1643, https://doi.org/10.1021/acsaem.9b02140.

[5] B. Zhu, Z. Liang, R. Zou, Designing advanced catalysts for energy conversion based on urea oxidation reaction, Small (2020), https://doi.org/10.1002/smll.201906133.

[6] D. Xu, Z. Fu, D. Wang, Y. Lin, Y. Sun, D. Meng, T. Feng Xie, A. Ni, OH)_2-modified Ti-doped α-Fe_2O_3 photoanode for improved photoelectrochemical oxidation of urea: the role of $Ni(OH)_2$ as a cocatalyst, Phys. Chem. Chem. Phys. 17 (2015) 23924–23930, https://doi.org/10.1039/c5cp03310a.

[7] J. Liu, J. Li, M. Shao, M. Wei, Directed synthesis of $SnO_2@BiVO_4/Co-P_i$ photoanode for highly efficient photoelectrochemical water splitting and urea oxidation, J. Mater. Chem. A 7 (2019) 6327–6336, https://doi.org/10.1039/c8ta11573g.

[8] S.A. Lee, S. Choi, C. Kim, J.W. Yang, S.Y. Kim, H.W. Jang, Si-based water oxidation photoanodes conjugated with earth-abundant transition metal-based catalysts, ACS Mater. Lett. 2 (2020) 107–126, https://doi.org/10.1021/acsmaterialslett.9b00422.

[9] G. Loget, Water oxidation with inhomogeneous metal-silicon interfaces, Curr. Opin. Colloid Interface Sci. 39 (2019) 40–50, https://doi.org/10.1016/j.cocis.2019.01.001.

[10] S.A. Lee, T.H. Lee, C. Kim, M.G. Lee, M.J. Choi, H. Park, S. Choi, J. Oh, H.W. Jang, Tailored NiO_x/Ni cocatalysts on silicon for highly efficient water splitting photoanodes via pulsed electrodeposition, ACS Catal. 8 (2018) 7261–7269, https://doi.org/10.1021/acscatal.8b01999.

[11] L.M. Peter, Photoelectrochemical water splitting. a status assessment, Electroanalysis 27 (2015) 864–871, https://doi.org/10.1002/elan.201400587.

[12] X. Zhou, R. Liu, K. Sun, K.M. Papadantonakis, B.S. Brunschwig, N.S. Lewis, 570 mV photovoltage, stabilized n-Si/CoO_x heterojunction photoanodes fabricated using atomic layer deposition, Energy Environ. Sci. 9 (2016) 892–897, https://doi.org/10.1039/c5ee03655k.

[13] S.A. Lee, T.H. Lee, C. Kim, M.J. Choi, H. Park, S. Choi, J. Lee, J. Oh, S.Y. Kim, H. W. Jang, Amorphous cobalt oxide nanowalls as catalyst and protection layers on n-type silicon for efficient photoelectrochemical water splitting, ACS Catal. 10 (2020) 420–429, https://doi.org/10.1021/acscatal.9b03899.

[14] M.J. Kenney, M. Gong, Y. Li, J.Z. Wu, J. Feng, M. Lanza, H. Dai, High-performance silicon photoanodes passivated with ultrathin nickel films for water oxidation, Science 342 (2013) 836–840, https://doi.org/10.1126/science.1241327.

[15] Y. Yu, C. Sun, X. Yin, J. Li, S. Cao, C. Zhang, P.M. Voyles, X. Wang, Metastable intermediates in amorphous titanium oxide: a hidden role leading to ultra-stable photoanode protection, Nano Lett. 18 (2018) 5335–5342, https://doi.org/10.1021/acs.nanolett.8b02559.

[16] A.G. Scheuermann, J.P. Lawrence, K.W. Kemp, T. Ito, A. Walsh, C.E.D. Chidsey, P. K. Hurley, P.C. McIntyre, Design principles for maximizing photovoltage in metal-oxide-protected water-splitting photoanodes, Nat. Mater. 15 (2016) 99–105, https://doi.org/10.1038/nmat4451.

[17] B. Liu, S. Feng, L. Yang, C. Li, Z. Luo, T. Wang, J. Gong, Bifacial passivation of: N -silicon metal-insulator-semiconductor photoelectrodes for efficient oxygen and

hydrogen evolution reactions, Energy Environ. Sci. 13 (2020) 221–228, https://doi.org/10.1039/c9ee02766a.

[18] Z. Luo, B. Liu, H. Li, X. Chang, W. Zhu, T. Wang, J. Gong, Multifunctional nickel film protected n-type silicon photoanode with high photovoltage for efficient and stable oxygen evolution reaction, Small Methods 3 (2019), https://doi.org/10.1002/smtd.201900212.

[19] Y.W. Chen, J.D. Prange, S. Dühnen, Y. Park, M. Gunji, C.E.D. Chidsey, P. C. McIntyre, Atomic layer-deposited tunnel oxide stabilizes silicon photoanodes for water oxidation, Nat. Mater. 10 (2011) 539–544, https://doi.org/10.1038/nmat3047.

[20] J. Hemmerling, J. Quinn, S. Linic, Quantifying losses and assessing the photovoltage limits in metal–insulator–semiconductor water splitting systems, Adv. Energy Mater. 10 (2020), https://doi.org/10.1002/aenm.201903354.

[21] I.A. Digdaya, G.W.P. Adhyaksa, B.J. Trześniewski, E.C. Garnett, W.A. Smith, Interfacial engineering of metal-insulator-semiconductor junctions for efficient and stable photoelectrochemical water oxidation, Nat. Commun. 8 (2017) 15968, https://doi.org/10.1038/ncomms15968.

[22] G. Loget, C. Mériadec, V. Dorcet, B. Fabre, A. Vacher, S. Fryars, S. Ababou-Girard, Tailoring the photoelectrochemistry of catalytic metal-insulator-semiconductor (MIS) photoanodes by a dissolution method, Nat. Commun. 10 (2019) 3522, https://doi.org/10.1038/s41467-019-11432-1.

[23] P. Aroonratsameruang, P. Pattanasattayavong, V. Dorcet, C. Mériadec, S. Ababou-Girard, S. Fryars, G. Loget, Structure-property relationships in redox-derivatized metal-insulator-semiconductor (MIS) photoanodes, J. Phys. Chem. C 124 (2020) 25907–25916, https://doi.org/10.1021/acs.jpcc.0c08971.

[24] J. Dabboussi, R. Abdallah, L. Santinacci, S. Zanna, A. Vacher, V. Dorcet, S. Fryars, D. Floner, G. Loget, Solar-assisted urea oxidation at silicon photoanodes promoted by an amorphous and optically adaptive Ni-Mo-O catalytic layer, J. Mater. Chem. A (2022), https://doi.org/10.1039/d2ta01212j.

[25] J.K. Bal, S. Kundu, S. Hazra, Hydrophobic to hydrophilic transition of HF-treated Si surface during Langmuir-Blodgett film deposition, Chem. Phys. Lett. 500 (2010) 90–95, https://doi.org/10.1016/j.cplett.2010.10.004.

[26] G. Kissinger, W. Kissinger, Hydrophilicity of Si wafers for direct bonding, Phys. Status Solidi A Appl. Mater. 123 (1991) 185, https://doi.org/10.1002/pssa.2211230117.

[27] X.F. Lu, X.Y. Chen, W. Zhou, Y.X. Tong, G.R. Li, α-Fe$_2$O$_3$@PANI core-shell nanowire arrays as negative electrodes for asymmetric supercapacitors, ACS Appl. Mater. Interfaces 7 (2015) 14843–14850, https://doi.org/10.1021/acsami.5b03126.

[28] L. Li, P. Ma, S. Hussain, L. Jia, D. Lin, X. Yin, Y. Lin, Z. Cheng, L. Wang, FeS$_2$/carbon hybrids on carbon cloth: a highly efficient and stable counter electrode for dye-sensitized solar cells, Sustain. Energy Fuels 3 (2019) 1749–1756, https://doi.org/10.1039/c9se00240e.

[29] R. Pai, A. Singh, S. Simotwo, V. Kalra, In situ grown iron oxides on carbon nanofibers as freestanding anodes in aqueous supercapacitors, Adv. Eng. Mater. 20 (2018), https://doi.org/10.1002/adem.201701116.

[30] J. Liu, E. Lee, Y.T. Kim, Y.U. Kwon, Ultra-high capacitance hematite thin films with controlled nanoscopic morphologies, Nanoscale 6 (2014) 10643–10649, https://doi.org/10.1039/c4nr03141e.

[31] Y. Kumar, A. Sharma, M.A. Ahmed, S.S. Mali, C.K. Hong, P.M. Shirage, Morphology-controlled synthesis and enhanced energy product (BH)$_{max}$ of CoFe$_2$O$_4$ nanoparticles, New J. Chem. 42 (2018) 15793–15802, https://doi.org/10.1039/c8nj02177e.

[32] H. Yao, J.A. Woollam, S.A. Alterovitz, Spectroscopic ellipsometry studies of HF treated Si (100) surfaces, Appl. Phys. Lett. 62 (1993) 3324–3326, https://doi.org/10.1063/1.109059.

[33] H. Zhang, Y. Lu, C.D. Gu, X.L. Wang, J.P. Tu, Ionothermal synthesis and lithium storage performance of core/shell structured amorphous@crystalline Ni-P nanoparticles, CrystEngComm 14 (2012) 7942–7950, https://doi.org/10.1039/c2ce25939g.

[34] X. Wang, B. Zhang, W. Zhang, M. Yu, L. Cui, X. Cao, J. Liu, Super-light Cu@Ni nanowires/graphene oxide composites for significantly enhanced microwave absorption performance, Sci. Rep. 7 (2017) 1584, https://doi.org/10.1038/s41598-017-01529-2.

[35] K. Zhang, X. Xia, S. Deng, Y. Zhong, D. Xie, G. Pan, J. Wu, Q. Liu, X. Wang, J. Tu, Nitrogen-doped sponge Ni fibers as highly efficient electrocatalysts for oxygen evolution reaction, Nano-Micro Lett. 11 (2019) 21, https://doi.org/10.1007/s40820-019-0253-5.

[36] N. Hao, Y. Wei, J. Wang, Z. Wang, Z. Zhu, S. Zhao, M. Han, X. Huang, In situ hybridization of an MXene/TiO$_2$/NiFeCo-layered double hydroxide composite for electrochemical and photoelectrochemical oxygen evolution, RSC Adv. 8 (2018) 20576–20584, https://doi.org/10.1039/c8ra02349b.

[37] X.L. Yang, Y.W. Lv, J. Hu, J.R. Zhao, G.Y. Xu, X.Q. Hao, P. Chen, M.Q. Yan, A three-dimensional nanostructure of NiFe(OH)$_x$ nanoparticles/nickel foam as an efficient electrocatalyst for urea oxidation, RSC Adv. 11 (2021) 17352–17359, https://doi.org/10.1039/d1ra01276b.

[38] I.A. Digdaya, B.J. Trześniewski, G.W.P. Adhyaksa, E.C. Garnett, W.A. Smith, General considerations for improving photovoltage in metal-insulator-semiconductor photoanodes, J. Phys. Chem. C 122 (2018) 5462–5471, https://doi.org/10.1021/acs.jpcc.7b11747.

[39] D.Y. Chung, P.P. Lopes, P. Farinazzo Bergamo Dias Martins, H. He, T. Kawaguchi, P. Zapol, H. You, D. Tripkovic, D. Strmcnik, Y. Zhu, S. Seifert, S. Lee, V. R. Stamenkovic, N.M. Markovic, Dynamic stability of active sites in hydr(oxy) oxides for the oxygen evolution reaction, Nat. Energy 5 (2020) 222–230, https://doi.org/10.1038/s41560-020-0576-y.

[40] Y. Pihosh, T. Minegishi, V. Nandal, T. Higashi, M. Katayama, T. Yamada, Y. Sasaki, K. Seki, Y. Suzuki, M. Nakabayashi, M. Sugiyama, K. Domen, Ta$_3$N$_5$-Nanorods enabling highly efficient water oxidation: via advantageous light harvesting and charge collection, Energy Environ. Sci. 13 (2020) 1519–1530, https://doi.org/10.1039/d0ee00220h.

[41] J.W. Yang, I.J. Park, S.A. Lee, M.G. Lee, T.H. Lee, H. Park, C. Kim, J. Park, J. Moon, J.Y. Kim, H.W. Jang, Near-complete charge separation in tailored BiVO$_4$-based heterostructure photoanodes toward artificial leaf, Appl. Catal. B Environ. 293 (2021), https://doi.org/10.1016/j.apcatb.2021.120217.

[42] H. Lee, J.W. Yang, J. Tan, J. Park, S.G. Shim, Y.S. Park, J. Yun, K. Kim, H.W. Jang, J. Moon, Crystal facet-controlled efficient SnS photocathodes for high performance bias-free solar water splitting, Adv. Sci. 2102458 (2021) 2102458, https://doi.org/10.1002/advs.202102458.

[43] R. Fan, S. Cheng, G. Huang, Y. Wang, Y. Zhang, S. Vanka, G.A. Botton, Z. Mi, M. Shen, Unassisted solar water splitting with 9.8% efficiency and over 100h stability based on Si solar cells and photoelectrodes catalyzed by bifunctional Ni-Mo/Ni, J. Mater. Chem. A 7 (2019) 2200–2209, https://doi.org/10.1039/c8ta10165e.

[44] S.A. Lee, I.J. Park, J.W. Yang, J. Park, T.H. Lee, C. Kim, J. Moon, J.Y. Kim, H. W. Jang, Electrodeposited heterogeneous nickel-based catalysts on silicon for efficient sunlight-assisted water splitting, Cell Rep. Phys. Sci. 1 (2020), 100219, https://doi.org/10.1016/j.xcrp.2020.100219.

[45] H. Park, I.J. Park, M.G. Lee, K.C. Kwon, S.P. Hong, D.H. Kim, S.A. Lee, T.H. Lee, C. Kim, C.W. Moon, D.Y. Son, G.H. Jung, H.S. Yang, J.R. Lee, J. Lee, N.G. Park, S. Y. Kim, J.Y. Kim, H.W. Jang, Water splitting exceeding 17% solar-to-hydrogen conversion efficiency using solution-processed Ni-based electrocatalysts and perovskite/Si tandem solar cell, ACS Appl. Mater. Interfaces 11 (2019) 33835–33843, https://doi.org/10.1021/acsami.9b09344.

[46] D. Kim, D. Joon Jung, I. Jae Park, B.W. Larson, S.P. Dunfield, C. Xiao, J. Kim, J. Tong, P. Boonmongkolras, S. Geun Ji, F. Zhang, S. Ryul Pae, M. Kim, S. Beom Kang, V. Dravid, J.J. Berry, J. Young Kim, K. Zhu, D. Hoe Kim, B. Shin, Efficient, stable silicon tandem cells enabled by anion-engineered wide-bandgap perovskites, Science 368 (2020) 155–160, https://doi.org/10.1126/science.aba3433.

[47] X. Hu, J. Zhu, J. Li, Q. Wu, Urea electrooxidation: current development and understanding of ni-based catalysts, ChemElectroChem 7 (2020) 3211–3228, https://doi.org/10.1002/celc.202000404.

[48] X. Ji, Y. Zhang, Z. Ma, Y. Qiu, Oxygen vacancy-rich Ni/NiO@NC nanosheets with schottky heterointerface for efficient urea oxidation reaction, ChemSusChem 13 (2020) 5004–5014, https://doi.org/10.1002/cssc.202001185.

[49] W. Xu, Z. Wu, S. Tao, Urea-based fuel cells and electrocatalysts for urea oxidation, Energy Technol. 4 (2016) 1329–1337, https://doi.org/10.1002/ente.201600185.